CHALMERS
UNIVERSITY OF TECHNOLOGY

Design and Verification of an Electrically Excited Synchronous Machine Rotor with Direct Oil Cooling for Truck Applications

Citation for the original published paper (version of record):
Boscaglia, L., Sugumar, H., Sharma, N. et al (2025). Design and Verification of an Electrically Excited Synchronous Machine Rotor with Direct Oil
Cooling for Truck Applications. IEEE Transactions on Transportation Electrification, 11(1): 236-245.
http://dx.doi.org/10.1109/TTE.2024.3389506

(article starts on next page)

Design and Verification of an Electrically Excited Synchronous Machine Rotor With Direct Oil Cooling for Truck Applications

Luca Boscaglia, *Member, IEEE*, Hari Sankar Natesan Sugumar, Nimananda Sharma, *Member, IEEE*, and Yujing Liu, *Senior Member, IEEE*

***Abstract*— The rotor cooling in electrically excited synchronous machines (EESMs) poses significant challenges due to the high power density resulting from active conductors necessary for generating the dc field, which in turn leads to substantial heat generation. Additionally, the rotor rotation further complicates the cooling system and contributes to mechanical losses. This article presents the design of the rotor cooling system for a 200 kW EESM for truck applications. The system employs simultaneous direct cooling of the hollow shaft, rotor lamination, and rotor winding using mineral oil. The design is verified in simulations using conjugate heat transfer (CHT) method by analyzing the oil flow and temperature distribution. Experimental tests are conducted on an eight-pole prototype rotor in stationary condition with a maximum coil heat loss of 4.7 kW, enabling 8 × 190 Aturns magneto-motive force (mmf) per pole with 9.2 L/min oil flow rate. The results demonstrate the effectiveness of the cooling method in doubling the possible current density for continuous operation, from 5.05 to 10.1 A/mm^2, keeping the *Start-up* condition for more than 5 min and the maximum power for 20 min when the ventilation effect for the rotor rotation is included in simulation.**

***Index Terms*— Direct oil rotor cooling, electric motors, electrically excited synchronous machine (EESM), heavy-duty trucks (HDTs), wound field synchronous machine (WFSM).**

I. Introduction

ELECTRIFICATION of heavy-duty trucks (HDTs) can significantly reduce the greenhouse gas (GHG) emissions. Although HDTs account for less than 5% of the vehicles on the road [1], they are responsible for approximately 20% of all carbon emissions within the transportation sector in the USA [2] and for a quarter of CO_2 emissions from road transport in the EU [3]. The advancement of HDT electrification has made significant progress in recent times, and McKinsey predicts that battery-electric HDT (BE HDT) could comprise around 15% of worldwide truck sales by 2030 [4]. However, the development of BE trucks is heavily limited by the low energy density and short cycle life of lithium-ion battery technology [5]. One approach to tackle this technological constraint is to mitigate vehicle energy consumption and battery aging by implementing highly efficient electric motors [6]. In a battery electric HDT, permanent magnet synchronous machines (PMSMs) convert the electrical energy stored in Li-ion batteries to propulsion torque. The lack of rare-earth permanent magnets (PMs), higher drive cycle efficiency [7], [8], and the ability to directly control the rotor flux make electrically excited synchronous machines (EESMs) an excellent alternative to PMSMs for HDT electrification. Since in EESMs the PMs are replaced with copper conductors, the dc excitation can be decreased in flux weakening reducing the supplied rotor current and leading to lower copper and iron loss compared to PMSMs. The higher efficiency and degree of control, as well as the lower environmental impact for the absence of PMs, are paid with the presence of extra components like the excitation circuit and the rotor cooling due to the drastic temperatures rise at field winding [9]. Additionally, it is worth noting that the EESM necessitates a power transfer device, such as high-maintenance brushes or a rotating transformer, to supply the required current to the rotor winding.

While the excitation typologies and control method are deeply investigated [10], [11], [12], [13], [14], there is a lack in the current literature related to effective cooling methods of the rotor for EESM and its challenges.

It is difficult to cool down the rotor in EESMs due to several reasons. First, the rotor winding of EESMs is subjected to high current density, leading to significant heating and a temperature rise. The heat generated in the rotor is transferred to the rotor core and shaft, which are usually made of high-quality magnetic materials such as laminated iron and steel, which have low thermal conductivity and high thermal capacity [15], [16]. This makes it difficult to extract the heat from the rotor and dissipate it effectively.

Second, the rotation of the rotor generates a centrifugal force that tends to push any direct coolant away from the rotor surface, reducing the cooling effectiveness. Furthermore, the rotational motion of the rotor does not allow any level of coolant at the air gap, otherwise the mechanical loss increases exponentially with the machine speed [17].

Various techniques are shown in Fig. 1 that can directly cool the rotor [18], [19], [20], [21]. Additionally, an overview of the recently published and accessible rotor cooling technologies is

Manuscript received 27 November 2023; revised 11 February 2024; accepted 12 March 2024. Date of publication 15 April 2024; date of current version 3 February 2025. This work was supported by European Union's Horizon 2020 Research and Innovation Programme under Grant 874972. *(Corresponding author: Luca Boscaglia.)*

The authors are with the Department of Electrical Engineering, Chalmers University of Technology, 41296 Gothenburg, Sweden (e-mail: luca.boscaglia@chalmers.se; sugumar@chalmers.se; sharman@chalmers.se; yujing.liu@chalmers.se).

Digital Object Identifier 10.1109/TTE.2024.3389506

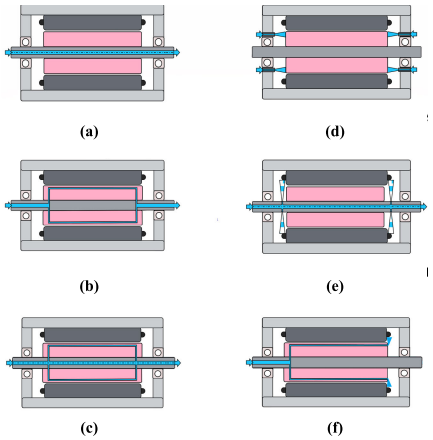

Fig. 1. Picture of different rotor cooling system designs for electric traction motors. (a) RSC. (b) DLCR. (c) RSC + DLCR. (d) RJIC. (e) RSC + radial rotor spray cooling (rRSpC). (f) LCR + rRSpC.

TABLE I
OVERVIEW OF ELECTRIC TRACTION MOTORS WITH DIFFERENT ROTOR COOLING DESIGN

Vehicle/Motor Model	Motor Typology	Peak Power [kW]	Rotor Cooling Typology
2018 Audi e-tron [23]	IMs	135/165	water-RSC
2018 Equipmake APM 200 [24] [25]	PMSM	220	Paratherm-DLCR
2018 Honda i-MMD Hybrid [26]	PMSM	135	ATF[a] -RSC+DLCR
2018 Rimac C-2 [27]	PMSMs	654/638	oil[b]-DLCR
2018 Tesla Model 3 [28] [29] [30]	PMSM	192	ATF-rRSpC
2019 GAC Aion S [31] [32]	PMSM	150	ATF-rRSpC
2019 Mercedes EQC [33] [34]	IMs	150	water-RSC
2020 Audi e-tron S [35] [36]	IMs	157/2x138	water-RSC
2021 Volkswagen ID CROZZ [37]	IM	75	oil-rRSPC
DOE-Project U.S. Drive [38]	EESM	80	ATF-RJIC
Ricardo UK Ltd [39]	PMSM	25	ATF-RSC+rRSPC

[a]ATF: Automatic Transmission Fluid.
[b]Mineral Oil.

listed in Table I. As shown in Fig. 1(a), the rotor lamination can be indirectly cooled through the coolant flowing inside the hollow shaft called rotor shaft cooling (RSC) [22], e.g., Audi e-tron and Mercedes EQC. The rotor lamination can be directly cooled using channels inside the lamination referred to as direct liquid cooled rotor (DLCR), e.g., Rimac C-2. As shown in Fig. 1(c), a combination of these two methods can also be used, e.g., Honda i-MMD Hybrid. However, both of these methods may be limited in cooling down the rotor of an EESM because of poor conductivity of heat from the winding to lamination and higher loss density. Therefore, direct cooling of the rotor winding may be preferred.

The direct cooling of the rotor can be achieved through rotor jet impingement cooling (RJIC) [40], [41], radial spray nozzles cooling (rRSpC), or a combination of them (DLCR + rRSpC) as shown in Fig. 1(d)–(e) [21]. The rRSpC method has been utilized in Tesla Model 3 to cool both the rotor and the end windings of the stator. This method utilizes the centrifugal force created by the rotation to spray liquid on the end winding, and the rotor lamination is indirectly cooled like RSC. Therefore, the effectiveness of end winding cooling depends on the machine's rotational speed. RJIC can overcome this shortcoming, as the coolant impinges via nozzles on the endplate. However, the lamination is not directly cooled in RJIC. A combination of DLCR and rRSpC is also proposed to cool the lamination and the stator end winding directly. However, in all three methods, the cooling of the rotor winding will be limited by the end winding surface area.

Therefore, this study presents a rotor cooling design in which oil directly comes into contact with the rotor active winding, lamination, and shaft simultaneously. The proposed design is also independent of the centrifugal force and could achieve efficient cooling even at low rotational speed. In addition, it should be mentioned that most of the current literature refers to oil cooling of the stator winding [42], [43], [44], [45] and a part of them to cooling of the rotor of PMSMs [22], [46], [47], [48], as well as air-cooled rotor (ACR) [49], while there is still a research gap on direct oil-cooled rotors for EESMs. For the mentioned reasons, the main novelty of this article is to propose, design, and verify a direct oil cooling method for an EESM rotor intended for truck application. The article is outlined as follows. The requirements of the application, machine specifications, and rotor cooling design are presented in Section I. It is followed by verification of the design using simulations in Section II. The modeling method is based on finite volume method (FVM) to build a conjugate heat transfer (CHT) model of the rotor. Section III presents experimental verification of the proposed design and the modeling method. Finally, the conclusion and future works are summarized in Section IV.

II. MACHINE REQUIREMENTS AND COOLING SYSTEM DESIGN

In this section, the target machine is introduced together with the requirements for heavy-duty truck application. The focus is on the design of the cooling system of the rotor under study.

A. Target Machine Requirements

The rotor considered in this study is part of a 200 kW EESM designed to fit the specifications of a two-motors drive-train for heavy-duty truck. The target machine torque, speed, and requirements for a single motor are shown in Fig. 2, which summarizes the typical operating points of an electric long haul truck [7], [50]. First, there is the *Start-up* condition that requires the maximum torque of the motors to accelerate the vehicle from a standstill while on a road with a slope 12%. *Climbing* is the maximum power operation and corresponds to driving uphill on a maximum slope of 6%. Finally, *Cruising* is highway driving at constant speed, typical for long-haul trucks, where the vehicle is supposed to have the best efficiency.

B. Target Machine Specifications

The target motor design parameters and specifications are listed in Table II. The stator winding consists of six layers and three-phase hairpin conductors with a maximum phase current amplitude of 350 A. The rotor is made up of eight salient poles mounted on the shaft, and the field winding, needed to create the dc excitation field, is wounded around each pole to create 190 turns. This number of turns and the maximum field current of 12 A create the mmf necessary to guarantee the desired maximum torque and power, as listed in Table II.

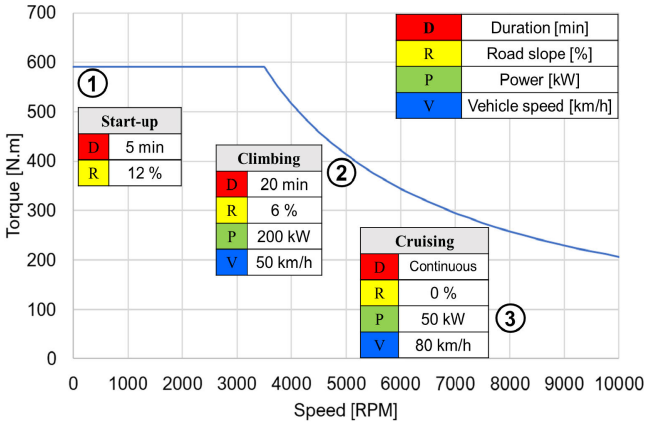

Fig. 2. Long haul electric truck drive-train operation requirements.

TABLE II
TARGET MACHINE PARAMETERS

Parameter	Value	Unit
Stator Outer Diameter	260	mm
Stator Inner Diameter	173	mm
Rotor Outer Diameter	171	mm
Stack Length	200	mm
Number of Poles	8	
Rotor Number of Turns	190	
Rotor Slot Fill Factor	40	%
Field Winding Resistance at 21°C	22.6	Ohm
Field Winding Insulation Class	180	°C
Maximum Torque	580	Nm
Maximum Power	210	kW
DC- Link Voltage	800	V
Maximum Speed	10000	rpm
Max Stator Current Amplitude	350	A
Max DC Rotor Current	12	A
Temperature of the coolant	45	°C

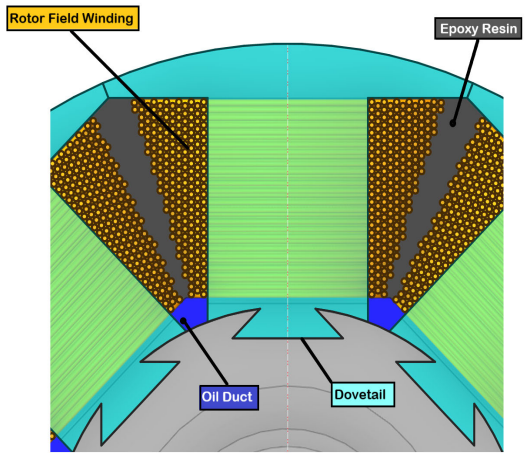

Fig. 3. Cross section of the rotor slot: the field conductors are wound around the poles up to certain limits due to manufacturing constrains. The empty bottom part of the rotor slot is used to derive an axial oil duct and a wedge is inserted to limit the oil spread to the airgap.

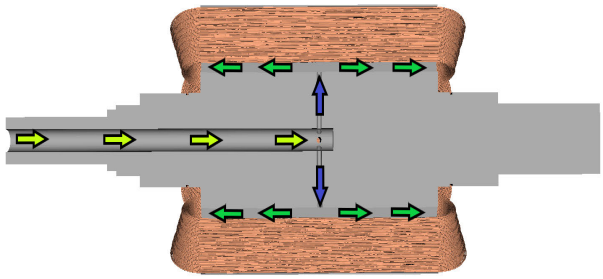

Fig. 4. Path of the oil inside the rotor cooling system: the oil is pumped through the hollow shaft (yellow arrows), the shaft radial channels (blue arrows), and it moves along the axial channels derived by the empty space at bottom part of the rotor slots (green arrows).

The electromagnetic design criterion is the achievement of the unitary power factor explained in detail in [51].

C. Rotor Design

In order to achieve reduced torque ripple, enhanced fill factor, and prevention of conductor displacement, the designed rotor adopts a closed slot design. The utilization of a closed slot design poses challenges in accommodating numerous conductors within the rotor. To address this, a dovetail joint is employed for assembling the rotor poles onto the shaft as shown in Fig. 3. This involves initially winding the rotor conductors around the poles, followed by mounting the poles onto the shaft using the dovetail joint.

The rotor cooling system is designed to enhance the dissipation of heat from the conductors by facilitating the oil flow along three main paths, as shown in Fig. 4. First, the oil is pressurized using a pump into the hollow shaft through a rotary joint, as indicated by yellow arrows. At the end of the shaft duct, eight smaller radial channels are created inside the shaft to push the oil outward, as shown by blue arrows. The oil flow in the radial direction is the result of pressurization and is also aided by centrifugal force during rotation. Since the space between the rotor poles cannot be filled entirely with copper conductors because of manufacturing limitations, part of this space shapes eight axial channels for oil passage, marked by green arrows. In this part, the oil comes in direct contact with the active conductors located at the bottom of the slot, as shown in Fig. 3. To prevent the oil from leaking toward the airgap, the rotor slot is filled with thermally conductive epoxy to better shape the cooling channels, which also aids in maintaining uniform oil pressure and velocity across all the ducts. After the oil flows out from the channels inside the rotor slots, it accumulates at the bottom of the housing, and it is then conveyed to the heat exchanger via a sucking pump.

III. FLOW AND THERMAL MODELING

This section describes the modeling of the oil flow inside the rotor and the CHT model implementation. In addition, the calculation of rotor losses used as input heat sources is also explained. The reason to build a CHT model at the design phase that includes both computational fluid dynamics (CFDs) and thermal calculation in steady state is to evaluate the cooling system effectiveness.

A. Loss Model

The reference current selection strategy is designed to minimize total copper losses, encompassing stator and rotor losses as described in [51]. The rotor losses are calculated by implementing a machine flux linkage-based model performing

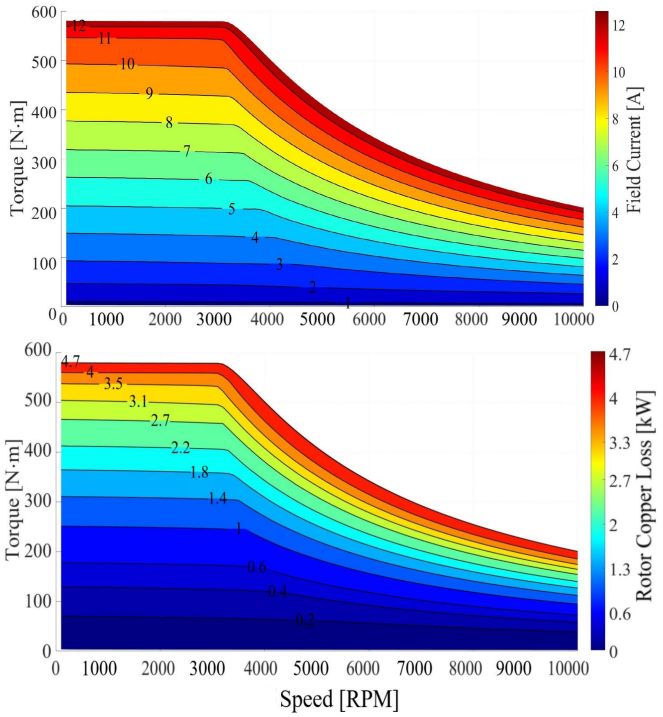

Fig. 5. Rotor field current and copper loss on the torque-speed plane calculated using FEM and MTPA algorithm.

a parametric sweep of rotor field current with a finite element model (FEM) in ANSYS Maxwell. Afterward, an iterative optimization method selects the field current to minimize the total copper losses. The total copper losses of the rotor and the field current for the entire torque-speed operating region of the machine are shown in Fig. 5. It can be observed from Figs. 2 and 5 that the maximum field current of 12 A is required to meet the start-up and climbing requirements, which correspond to a loss of 4.7 kW in the rotor winding. Furthermore, a field current of 5 A is needed to meet the cruising requirement, corresponding to a loss of 0.8 kW, which is almost six times smaller.

B. Steady-State CHT Model

Given the symmetry of the geometry, only one-eighth of the rotor is imported for the analysis including one salient pole, one-eighth of the shaft, all the 190 field copper conductors and their insulation with high fidelity. The oil channels are extracted from the solids and set as fluid, and the following assumptions are made.

1) The thermal conductivity of the rotor is set as anisotropic due to the lamination and all the thermal properties of the materials are listed in Table III.
2) The kinetic viscosity and density of the oil are considered as functions of the local temperature using the following equations derived from the ExxonMobil[1] data sheet:

$$\rho = 864 - 44T \tag{1}$$

$$\nu = -20 + 70T - 10T^2 \tag{2}$$

[1]Registered trademark.

TABLE III
THERMAL PROPERTIES OF THE MACHINE COMPONENTS

Component	Thermal Conductivity [W/mK]	Specific Heat [J/(kg K)]
Lamination (radial)	45	460
Lamination (axial)	34	502
Shaft (Stainless Steel)	50	460
Copper	387.6	381
Winding Insulation	0.18	1000
Epoxy Resin	0.68	1138

where ρ is the fluid density in kg/m^3, and ν the kinematic viscosity in *cst* and T the local temperature of the oil.

3) The input copper loss calculated in Fig. 5 is considered a function of the local temperature using the following relation:

$$P_{\mathrm{cu},T} = P_{\mathrm{cu},T_0}[1 + \alpha(T - T_0)] \tag{3}$$

where $P_{\mathrm{cu},T}$ is the corrected copper loss that is updated for each temperature T obtained from each steady-state simulation, the P_{cu,T_0} is the copper loss when the field winding resistance is measured at reference temperature T_0, and α is the thermal coefficient of the copper.

4) The *Frozen Rotor* approach is employed to simulate the rotation of the rotor by selecting the surfaces of the rotor winding and lamination that are in direct contact with the air. This method enables the Coriolis acceleration and centripetal acceleration to be solved when the *Frame Motion* is activated on those walls, thus eliminating the need for costly transient simulations and allowing the rotor rotation to be simulated in a steady-state.
5) Rotating the rotor would provide extra cooling on the end windings, as some of the oil would come in contact with them. However, the effect of the oil at the end winding is neglected in the steady-state simulations.

The pressure–velocity *coupled* solver is utilized in ANSYS Fluent to improve result accuracy, particularly in rotating machines where pressure and velocity calculations are intricately linked. Additionally, the $k - \omega$ turbulence model is applied to better capture turbulence effects. In Fig. 6, the simulation results are displayed at 8 A and 9.2 L/min as temperature contours along the axial and radial direction. Under standstill conditions, the maximum temperature is attained in the outermost section of the end winding, where the stationary surrounding air acts as a barrier, limiting the heat dissipation. The bottom side of the field winding, which is in direct contact with the oil channels, experiences a significant cooling effect, resulting in a temperature reduction by half, from approximately 148 °C to around 75 °C. The presence of the oil channels also results in a nonuniform temperature distribution across the rotor lamination in the radial direction, leading to a temperature difference of approximately 30°. Furthermore, a noticeable temperature disparity arises due to the air gap within the dovetail joint connecting the rotor lamination and the shaft, where the temperature is primarily influenced by the oil temperature.

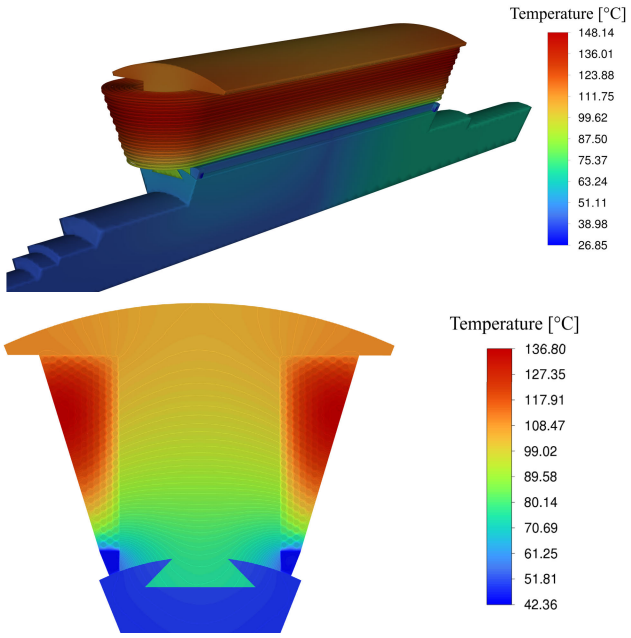

Fig. 6. Temperature contours from the steady-state CHT model simulating one-eighth of the rotor in standstill condition with 8 A field current and 9.2 L/min oil flow rate.

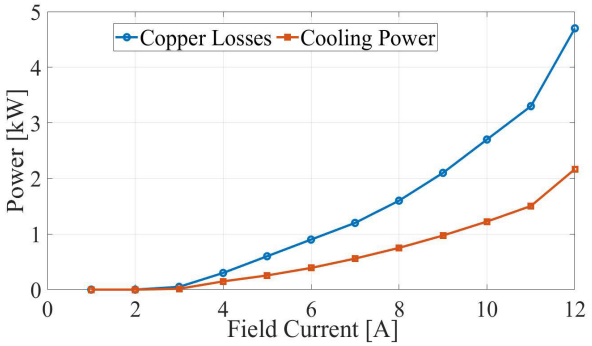

Fig. 7. Copper losses and power dissipated by the cooling system for different values of the rotor field current.

In Fig. 7, the dissipated power throughout the entire oil cooling system is estimated in the ANSYS Fluent from the surface average heat flux of the oil ducts. The cooling system capability is compared with total rotor copper losses and plotted as function of the field winding current. It is evident that the oil is capable of dissipating a maximum power from the rotor slightly below 2.5 kW, representing approximately half of the total rotor copper losses. This discrepancy diminishes as the rotor current decreases.

IV. Simulations and Experimental Results

In the laboratory, a prototype of the rotor is tested at various copper losses and flow rates, simulating the worst-case scenario of operation. This scenario is characterized by the rotor being at a standstill without any ventilation or oil spread to aid in the cooling of the end winding. The pressure drop and temperature at different points on the rotor are measured and compared with the simulation results. The primary focus is on the winding temperatures at three typical operating points of an electric long-haul truck, as shown in Fig. 2.

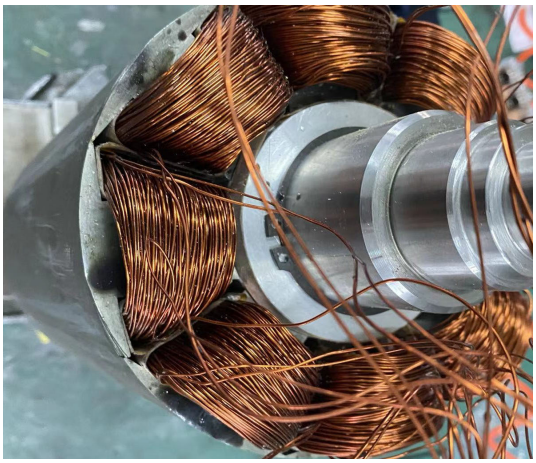

Fig. 8. Image of the prototype rotor following the winding of the field conductors.

Fig. 9. Image of the prototype rotor postapplication of epoxy resin, fiberglass bandage, and extra material for balancing.

A. Rotor Manufacturing

The EESM rotor comprises two primary components: a solid hollow shaft made of stainless steel, with cooling channels drilled along both axial and radial directions as described in Section II-C, and the poles in laminated electric steel. The assembling of the prototype rotor is distinguished by three key processes: the implementation of field winding, the mounting of the poles onto the shaft, and the potting process using epoxy resin. The conductors are individually wound around each laminated rotor pole and subsequently interconnected in series. This methodology enables the attainment of an elevated fill factor through the utilization of closed slots before assembling the poles onto the shaft, as illustrated in Fig. 8. Once the rotor assembling is completed, a bandage made of fiberglass is employed around the rotor end winding to prevent the conductors displacement at high speed. Fiberglass, chosen for its mechanical strength, securely holds the rotor conductors in place during operation. Subsequently, the entire structure is filled with epoxy resin to enhance

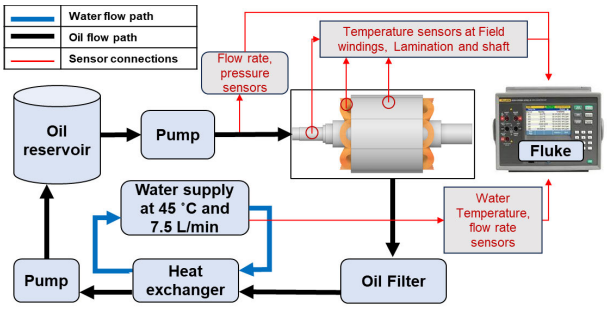

Fig. 10. Schematic of the oil cooling setup used for experimental measurements.

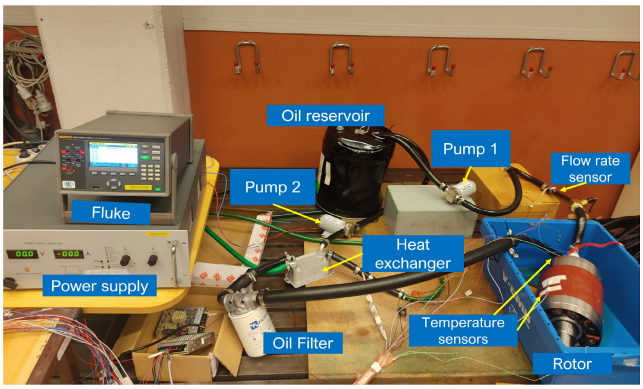

Fig. 11. Picture of the oil cooling setup used for experimental measurements.

compactness and define the oil cooling channels between the rotor winding with greater precision, as shown in Fig. 9.

B. Experimental Setup

The laboratory setup illustrated in the schematic in Fig. 10 and shown in Fig. 11 is used to investigate the effectiveness of the proposed cooling system. The cooling circuit comprises two gear pumps, an oil reservoir, a heat exchanger, an oil filter, and power sources for the pumps and field excitation. The first pump delivers the oil from the reservoir to the rotor shaft, whereas the second pump sucks the oil into the oil filter and heat exchanger. The rotor is placed in a plastic box and elevated through wood supports in order to thermally insulate the lamination. Throughout the thermal experiments, the flow rate of the oil is maintained at 9.2 L/min, and the flow rate of water to cool the oil in the heat exchanger at 7.5 L/min. The temperature of the water is kept at 45 °C to simulate the temperature of the water in the truck. Several sensors are used inside the setup: a pressure transducer to measure the oil pressure drop along the rotor cooling system, two flow rate sensors Swissflow SF-800 to ensure the correct values of oil and water flow rates, the temperature of both the oil and water is measured at the inlet and outlet of the heat exchanger, as well as at the rotor, to ensure that the fluids are maintained at the desired temperatures. Five thermocouples are used to measure the temperature of the shaft, rotor lamination, and field winding at three different positions. The locations of the thermocouples are shown in Fig. 12. Sensor 1 is on the end winding since that position corresponds to the rotor hot spot, as can be deduced from Fig. 6. Sensor 2 and Sensor 3 are located on the coil side in proximity of the oil path, with an axial depth of 20 mm from the rotor outer face. Sensor 4 is on the nondrive end side of the shaft, whereas Sensor 5 is on the rotor outer surface. The field excitation system is controlled in order to keep the current at constant value and emulate the actual operation of the machine at different copper losses.

C. CHT Model Verification

Experimental tests are conducted to validate the CHT model and assess the effectiveness of the cooling method. Initially, the fluid dynamics model is verified by measuring the pressure throughout the entire rotor cooling system. This involves recording the pressure at the rotor inlet while varying the oil flow rates. Given that the pressure at the rotor outlet is

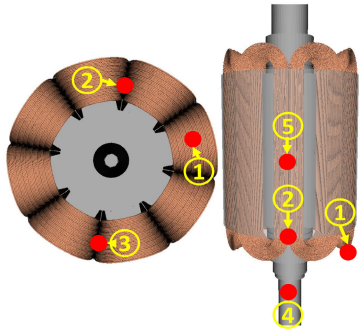

Fig. 12. Location of temperature sensors: Sensor 1 is located at end winding (hotspot); Sensor 2 and Sensor 3 are located on the coil sides with an axial depth of 20 mm from the rotor outer face and respectively at rotor top side and bottom side; Sensor 4 is on the shaft, and Sensor 5 is on the outer surface of the rotor lamination.

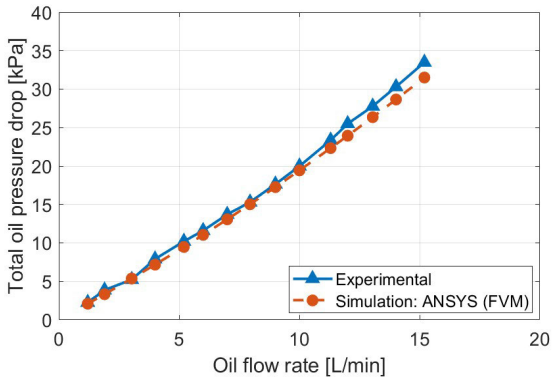

Fig. 13. Total pressure drops along the rotor cooling system as function of the oil flow rate while the rotor is not excited at room temperature. Both experimental measurements (blue) and simulations in ANSYS Fluent using FVM (red) are shown.

zero, the inlet pressure corresponds to the entire pressure drop. In Fig. 13, the static pressure drop is plotted as a function of the inlet oil flow rate. In particular, the results show a minimum pressure drop of 2.5 kPa at 1 L/min and a maximum pressure drop of approximately 35 kPa at 15 L/min, with the oil temperature maintained at a constant 45 °C. Importantly, the experimental data closely aligns with the CFD simulation, with an error margin of less than 5%. Subsequently, thermal tests are conducted by varying the rotor current to simulate copper losses at different operational points of the machine.

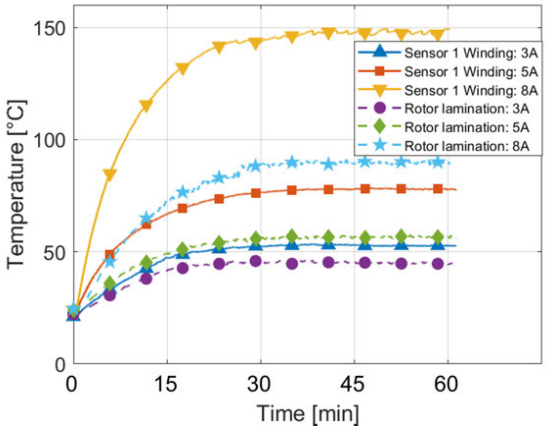

Fig. 14. Temperature of the end winding (Sensor 1) and lamination after 60 min (steady state). Direct oil cooling is activated and field current is set at three different values of 3, 5 and 8 A.

In Fig. 14, the recorded temperatures for the end winding, which is expected to reach the highest temperatures, and the rotor lamination are presented. These measurements are taken at three different rotor current values: 3, 5, and 8 A, over a 60-min testing duration. It is noteworthy that the temperature exhibits a characteristic first-order thermal circuit behavior, reaching a steady-state value after approximately 40 min.

Fig. 15 illustrates the temperatures of the field winding, rotor lamination, and shaft once they reach steady-state conditions after 60 min of testing, across a range of rotor current values from 3 to 8 A, corresponding to rotor current densities ranging from 3.18 to 11.4 A/mm^2. The values of temperature are then compared with the ones obtained from the CHT steady-state simulations in ANSYS Fluent. Notably, Sensor 1 records the highest temperature, as anticipated, at the rotor end winding. On the contrary, Sensor 3 registers the lowest temperature due to its proximity to the oil channel and its location at the lower section of the rotor, where it also benefits from gravity-assisted oil flow from channels situated on the upper side.

Sensor 2, which is not affected by these effect, records a higher temperature. Both the rotor winding and rotor lamination exhibit a power-law relationship with increasing field current, resulting in rising temperatures. On the contrary, the temperature of the hollow shaft remains largely unaffected by the rotor current, primarily influenced by the coolant temperature, which is maintained at approximately 45°. In this case as well, a maximum deviation of 5% is observed between the experimental and simulation results. The deviation is mainly due to aleatory factors related to the sensors positioning and gluing during the manufacturing process.

A further test is conducted to investigate the effect of the flow rates on the cooling effectiveness of the system. The test involved varying the inlet oil flow rate within a range from 7 to 13 L/min while maintaining a consistent current in the field winding of 5 A. The resulting temperatures from this test are presented in Fig. 16, along with the maximum temperature variation observed. Sensor 2 and Sensor 3 are the most affected by changes in flow rate due to their proximity to the cooling channels, exhibiting maximum temperature

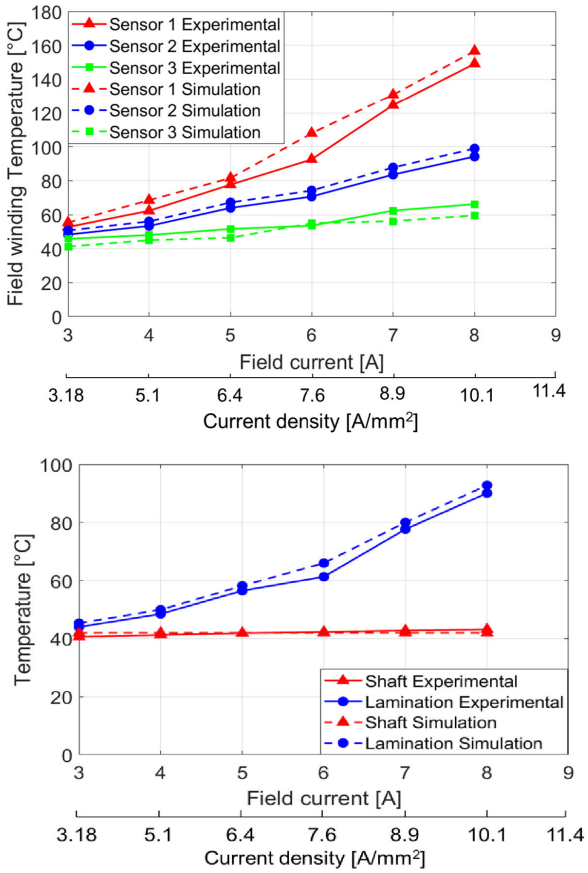

Fig. 15. Comparison between experimental and simulation results of the steady-state temperatures with direct-oil cooling.

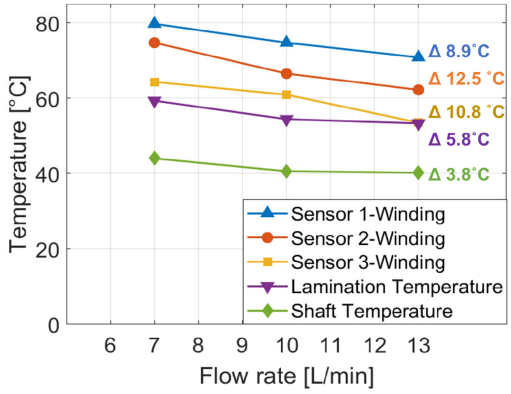

Fig. 16. Temperature of the field winding, lamination, and shaft varying the oil flow rate at constant field current of 5 A. The Δ gives the temperature difference between the lowest and highest flow rate values.

variations of 12.5 °C and 10.8 °C, respectively. Sensor 1 is also significantly affected, displaying a maximum temperature variation of 10.8 °C. In contrast, the flow rate has a minimal impact on the lamination and shaft temperatures, with maximum variations of 5.8 °C and 3.8 °C, respectively.

D. HDT Requirements

Experiments are carried out at different values of rotor current and different test duration with the aim to validate compliance with the requirements for HDT, specifically at the

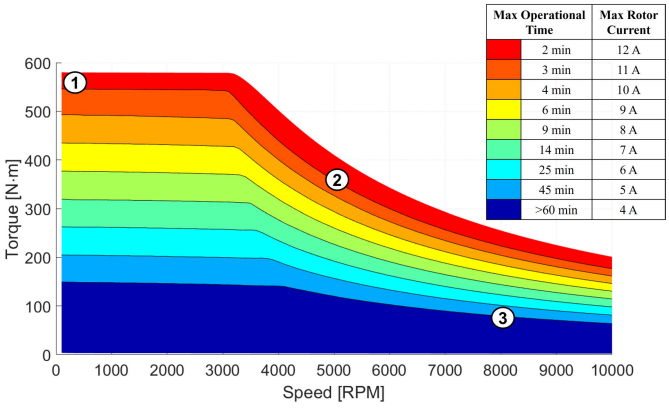

(a)

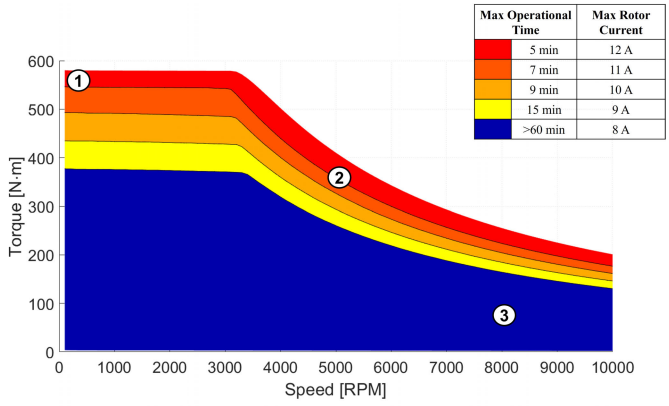

(b)

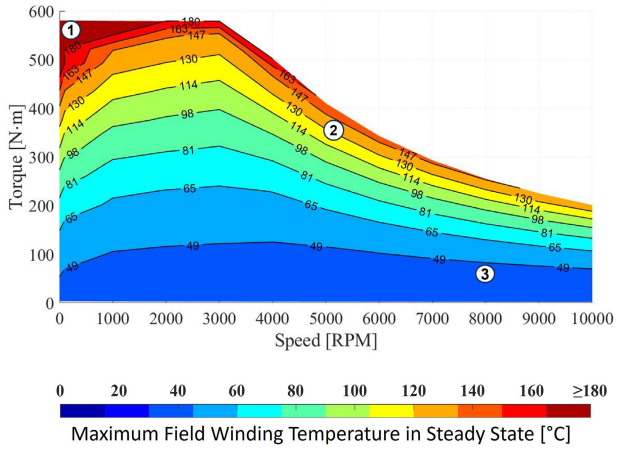

(c)

Fig. 17. (a) and (b) Maximum operational time before reaching the insulation class limit of 180 °C along the torque-speed map from experimental measurements and (c) maximum steady-state temperature of the field winding from simulations. The water temperature at the heat exchanger is kept around 45 °C.

three typical operating points detailed in Fig. 2: (1) *Start-up*; (2) *Climbing*; (3) *Cruising*.

Fig. 17 presents the results along the torque-speed map for different scenarios. In Fig. 17(a)–(b), the experimental results are presented and the different colors represent the maximum operating duration in that specific region before meeting the critical temperature of 180 °C imposed by the insulation class of the rotor conductors. Additionally, each of the colors represents an operating region of the motor with a specific rotor current needed to reach the corresponding amount of torque. To clarify further, in Fig. 17(a), the experiments are conducted without the application of direct oil cooling, and the rotor is maintained in a stationary state.

This condition represents the worst-case scenario and only the requirements for the continuous operation (3) are partially met, where the truck in that point is supposed to run continuously. In Fig. 17(b), experiments are carried out activating the direct oil cooling system and considering the rotor in a standstill. It can be seen that the blue region, which represents the area where the truck can run for a very long time, is enlarged due to the influence of oil cooling. Consequently, the rotor current that can be kept continuously is doubled from 4 to 8 A, doubling also the corresponding torque accordingly. This expansion results in meeting the requirements for *Start-up* and *Cruising* However, the *Climbing* requirement is not entirely satisfied. In point (3), the truck can run indefinitely with the aid of oil cooling and it can operate for 5 min in point (1). In contrast, it cannot maintain operation for 20 min at point (3) since the field winding insulation would begin to deteriorate after 7 min due to the elevated temperature.

In Fig. 17(c), the CHT model is used to run extensive simulations covering the entire torque-speed map of the machine. In this scenario, both the oil cooling and the ventilation effect due to the rotor rotation are activated and the color map represents the maximum temperature reached in steady-state by the field winding, which is the component of the machine subject to the highest temperatures. The red color demarcates the region where the truck cannot operate for long time (steady state), as the temperature of the rotor conductors would exceed the maximum limit imposed by the insulation class. It is noteworthy that the region where the truck can operate indefinitely is significantly expanded compared to Fig. 17(b), showing a further increase in rotor current in the continuous region from 8 to 10 A accompanied by a decrease in temperature correlated with the speed increase. This enhancement guarantees the fulfillment of requirements even during *Climbing*. Consequently, the proposed cooling method effectively meets all the requirements for HDTs.

V. Conclusion

This article proposes a novel design for an EESM direct oil-cooled rotor for HDT, where the performance and requirements are validated through simulations and experiments. Experimental verifications have shown that the rotor can remain stationary up to a current of 8 A, which is equivalent to a current density of 10.1 A/mm^2. This implies that the direct oil cooling method proposed doubles the current density for continuous operation, from 5.05 to 10.1 A/mm^2. Due to the advantages of oil cooling, the amount of time spent on *Start-up* is more than doubled from 2 to 5 min, whereas for *Climbing*, it is increased from 4 to 7 min. Although the machine has been tested in stationary condition, the rotation of the rotor is simulated using a CHT model importing the losses obtained from the FEM electromagnetic calculations. The CHT model indicates that when the rotor is rotating, the area of continuous operation of the machine is enlarged in

simulations and also the target of 20 min of operation for the *Climbing* is widely achieved. The model is validated with experimental results proving to estimate the temperatures with high accuracy, within the 5% error. This error arises primarily from factors such as the presence of glue and epoxy, along with uncertainties related to the positioning of sensors during the manufacturing process.

REFERENCES

[1] *Number of Vehicles and Gallons of Fuel*, U.S. Dept. Transp., Federal Highway Admin., Washington, DC, USA, Dec. 2014.

[2] D. C. Quiros, J. Smith, A. Thiruvengadam, T. Huai, and S. Hu, "Greenhouse gas emissions from heavy-duty natural gas, hybrid, and conventional diesel on-road trucks during freight transport," *Atmos. Environ.*, vol. 168, pp. 36–45, Nov. 2017.

[3] (Apr. 2023). *Reducing Greenhouse Gas Emissions From Heavy-Duty Vehicles in Europe*. [Online]. Available: https://www.eea.europa.eu/publications/co2-emissions-of-new-heavy

[4] C. Tryggestad, N. Sharma, J. van de Staaij, and A. Keizer. (2017). *New Reality: Electric Trucks and Their Implications on Energy Demand*. McKensey Energy Insights. [Online]. Available: https://www.mckinsey.com/industries/oil-and-gas/our-insights/a-new-reality-electric-trucks

[5] S. Sripad and V. Viswanathan, "Performance metrics required of next-generation batteries to make a practical electric semi truck," *ACS Energy Lett.*, vol. 2, no. 7, pp. 1669–1673, Jul. 2017.

[6] D. Smith et al., "Medium- and heavy-duty vehicle electrification: An assessment of technology and knowledge gaps," U.S. Dept. Energy, Office Energy Efficiency Renew. Energy, USA, 2020, doi: 10.2172/1615213.

[7] G. Mademlis, Y. Liu, J. Tang, L. Boscaglia, and N. Sharma, "Performance evaluation of electrically excited synchronous machine compared to PMSM for high-power traction drives," in *Proc. Int. Conf. Electr. Mach. (ICEM)*, vol. 1, Aug. 2020, pp. 1793–1799.

[8] Z. Q. Zhu, W. Q. Chu, and Y. Guan, "Quantitative comparison of electromagnetic performance of electrical machines for HEVs/EVs," *CES Trans. Electr. Mach. Syst.*, vol. 1, no. 1, pp. 37–47, Mar. 2017.

[9] E. Wang, P. Grabherr, P. Wieske, and M. Doppelbauer, "A low-order lumped parameter thermal network of electrically excited synchronous motor for critical temperature estimation," in *Proc. Int. Conf. Electr. Mach. (ICEM)*, Sep. 2022, pp. 1562–1568.

[10] J. Tang, Y. Liu, and N. Sharma, "Modeling and experimental verification of high-frequency inductive brushless exciter for electrically excited synchronous machines," *IEEE Trans. Ind. Appl.*, vol. 55, no. 5, pp. 4613–4623, Sep. 2019.

[11] Y. Han, X. Wu, G. He, Y. Hu, and K. Ni, "Nonlinear magnetic field vector control with dynamic-variant parameters for high-power electrically excited synchronous motor," *IEEE Trans. Power Electron.*, vol. 35, no. 10, pp. 11053–11063, Oct. 2020.

[12] J. Tang, Y. Liu, and S. Lundberg, "Estimation algorithm for current and temperature of field winding in electrically excited synchronous machines with high-frequency brushless exciters," *IEEE Trans. Power Electron.*, vol. 36, no. 3, pp. 3512–3523, Mar. 2021.

[13] J. Kou, Q. Gao, Y. Teng, J. Ye, and D. Xu, "An envelope-prediction-based sensorless rotor position observation scheme for LCI-fed EESM at zero and low speed," *IEEE Trans. Power Electron.*, vol. 35, no. 7, pp. 7356–7365, Jul. 2020.

[14] R. Manko, M. Vukotic, D. Makuc, D. Miljavec, and S. Corovic, "Study of the dynamic performance of an electrically excited synchronous machine with rotary transformer," in *Proc. IEEE Int. Conf. Modern Electr. Energy Syst. (MEES)*, Sep. 2021, pp. 1–5.

[15] D. Staton, A. Boglietti, and A. Cavagnino, "Solving the more difficult aspects of electric motor thermal analysis in small and medium size industrial induction motors," *IEEE Trans. Energy Convers.*, vol. 20, no. 3, pp. 620–628, Sep. 2005.

[16] D. Liang et al., "Influence of critical parameters in lumped-parameter thermal models for electrical machines," in *Proc. 22nd Int. Conf. Electr. Mach. Syst. (ICEMS)*, Aug. 2019, pp. 1–6.

[17] L. Boscaglia, Y. Liu, H. Avsar, J. Tang, and M. Galbiati, "Convective heat transfer coefficients and mechanical loss evaluation of oil splashing in direct cooled electrically excited hairpin motors," in *Proc. Int. Conf. Electr. Mach. (ICEM)*, Sep. 2022, pp. 496–503.

[18] Y. Gai et al., "Cooling of automotive traction motors: Schemes, examples, and computation methods," *IEEE Trans. Ind. Electron.*, vol. 66, no. 3, pp. 1681–1692, Mar. 2019.

[19] P.-O. Gronwald and T. A. Kern, "Traction motor cooling systems: A literature review and comparative study," *IEEE Trans. Transport. Electrific.*, vol. 7, no. 4, pp. 2892–2913, Dec. 2021.

[20] A. J. Bourgault, P. Roy, E. Ghosh, and N. C. Kar, "A survey of different cooling methods for traction motor application," in *Proc. IEEE Can. Conf. Electr. Comput. Eng. (CCECE)*, May 2019, pp. 1–4.

[21] P. S. Ghahfarokhi, A. Podgornovs, A. Kallaste, A. J. M. Cardoso, A. Belahcen, and T. Vaimann, "The oil spray cooling system of automotive traction motors: The state of the art," *IEEE Trans. Transport. Electrific.*, vol. 9, no. 1, pp. 428–451, Mar. 2023.

[22] Y. Gai et al., "Numerical and experimental calculation of CHTC in an oil-based shaft cooling system for a high-speed high-power PMSM," *IEEE Trans. Ind. Electron.*, vol. 67, no. 6, pp. 4371–4380, Jun. 2020.

[23] J. Doerr, T. Attensperger, L. Wittmann, and T. Enzinger, "The new electric axle drives from audi," *MTZ worldwide*, vol. 79, no. 6, pp. 18–25, Jun. 2018, doi: 10.1007/s38313-018-0042-4.

[24] (2020). *Datasheet APM 200*. [Online]. Available: https://equipmake.co.uk/wp-content/uploads/2018/07/apm200-data.pdf

[25] G. Volpe, J. Goss, I. Foley, F. Marignetti, M. Popescu, and D. A. Staton, "High-performance electric motor for motor sport application," in *Proc. IEEE Vehicle Power Propuls. Conf. (VPPC)*, Dec. 2017, pp. 1–5.

[26] Y. Ito, T. Aoki, T. Naito, and T. Hiranishi, "Development of motor with heavy rare Earth-free magnet for two-motor hybrid system," *SAE Int. J. Adv. Current Practices Mobility*, vol. 1, no. 3, pp. 1169–1176, Apr. 2019, doi: 10.4271/2019-01-0600.

[27] (Dec. 2020). *Rimac Automobili Powertrain System*. [Online]. Available: http://offthegridsun.com/RA_Motors_Detailed.pdf

[28] (Dec. 2020). *What Engineers Found When They Tore Apart Tesla's Model 3*. [Online]. Available: https://www.youtube.com/watch?v=Lj1a8rdX6DU

[29] (Dec. 2020). *Tesla Model 3: Inside & Out-Autoline After Hours 417*. [Online]. Available: https://www.youtube.com/watch?v=CpCrkO1x-Qo

[30] (Mar. 2020). *Automotive Benchmarking*. [Online]. Available: https://portal.a2mac1.com/

[31] A. K. M. Özbek, J. Trommer, and Y. Yosuke, "Nidec next generation electric traction motor," in *Proc. VDI Int.*, 2019, pp. 77–84.

[32] C. Hampel. (Dec. 2020). *GAC Aion S Electric Car First to Get Nidec E-Axle*. [Online]. Available: https://www.electrive.com/2018/12/10/gacs-aion-s-e-limosine-gets-a-nidec-electric-axel/

[33] M. Jordan. (Dec. 2020). *Blick Auf Das Neu Entwickelte Antriebssystem Des EQC*. [Online]. Available: https://blog.mercedes-benz-passion.com/2018/09/blick-auf-das-neu-entwickeltes-antriebssystem-des-eqc-switchtoeq-eq/

[34] C. Brunglinghaus. (Dec. 2020). *Vollintegrierter Elektrischer ZF-Achsantrieb Geht 2018 in Serie*. [Online]. Available: https://www.springerprofessional.de/antriebsstrang/vollintegrierter-elektrischer-zf-achsantrieb-geht-2018-in-serie-/7498340

[35] J. Doerr, G. Fröhlich, A. Stroh, and M. Baur, "Das elektrische antriebssystem mit drei-motor-layout im Audi e-tron S," *MTZ Motortechnische Zeitschrift*, vol. 81, nos. 7–8, pp. 18–27, Jul. 2020.

[36] J. Doerr et al., "Das elektrische antriebssystem mit 3-motor-layout im Neuen audi e-tron top-modell: The electric drivetrain with 3-motor-layout of the new Audi e-tron top model," *Internationales Wiener Motorensymp.*, vol. 81, pp. 18–27, Jul. 2020.

[37] D.-I. C. Helbing et al., "The powertrain of the ID.4—Volkswagen expands the portfolio of the MEB," in *Proc. 41st Int. Vienna Motor Symp.*, Fortschritt-Berichte VDI, 2019.

[38] A. Di Gioia et al., "Design and demonstration of a wound field synchronous machine for electric vehicle traction with brushless capacitive field excitation," *IEEE Trans. Ind. Appl.*, vol. 54, no. 2, pp. 1390–1403, Mar. 2018.

[39] A. D. Wearing, J. Haybittle, R. Bao, J. W. Baxter, C. Rouaud, and O. Taskin, "Development of high power 48 V powertrain components for mild hybrid light duty vehicle applications," in *Proc. IEEE Energy Convers. Congr. Expo. (ECCE)*, Sep. 2018, pp. 3893–3900.

[40] C. Liu et al., "Experimental investigation of oil jet cooling in electrical machines with hairpin windings," *IEEE Trans. Transport. Electrific.*, vol. 9, no. 1, pp. 598–608, Mar. 2023.

[41] C. Liu et al., "Estimation of oil spray cooling heat transfer coefficients on hairpin windings with reduced-parameter models," *IEEE Trans. Transport. Electrific.*, vol. 7, no. 2, pp. 793–803, Jun. 2021.

[42] C. Liu et al., "Experimental investigation on oil spray cooling with hairpin windings," *IEEE Trans. Ind. Electron.*, vol. 67, no. 9, pp. 7343–7353, Sep. 2020.
[43] Y. Liu, Z. Zhang, C. Wang, W. Geng, and T. Yang, "Design and analysis of oil-immersed cooling stator with nonoverlapping concentrated winding for high-power ironless stator axial-flux permanent magnet machines," *IEEE Trans. Ind. Electron.*, vol. 68, no. 4, pp. 2876–2886, Apr. 2021.
[44] R. Camilleri, P. Beard, D. A. Howey, and M. D. McCulloch, "Prediction and measurement of the heat transfer coefficient in a direct oil-cooled electrical machine with segmented stator," *IEEE Trans. Ind. Electron.*, vol. 65, no. 1, pp. 94–102, Jan. 2018.
[45] R. Camilleri, D. A. Howey, and M. D. McCulloch, "Predicting the temperature and flow distribution in a direct oil-cooled electrical machine with segmented stator," *IEEE Trans. Ind. Electron.*, vol. 63, no. 1, pp. 82–91, Jan. 2016.
[46] A. Acquaviva, S. Skoog, and T. Thiringer, "Design and verification of in-slot oil-cooled tooth coil winding PM machine for traction application," *IEEE Trans. Ind. Electron.*, vol. 68, no. 5, pp. 3719–3727, May 2021.
[47] P. Lindh et al., "Direct liquid cooling method verified with an axial-flux permanent-magnet traction machine prototype," *IEEE Trans. Ind. Electron.*, vol. 64, no. 8, pp. 6086–6095, Mar. 2017.
[48] W. Li, Z. Cao, and X. Zhang, "Thermal analysis of the solid rotor permanent magnet synchronous motors with air-cooled hybrid ventilation systems," *IEEE Trans. Ind. Electron.*, vol. 69, no. 2, pp. 1146–1156, Feb. 2022.
[49] W. Li, D. Li, J. Li, and X. Zhang, "Influence of rotor radial ventilation ducts number on temperature distribution of rotor excitation winding and fluid flow state between two poles of a fully air-cooled hydro-generator," *IEEE Trans. Ind. Electron.*, vol. 64, no. 5, pp. 3767–3775, May 2017.
[50] L. Boscaglia, N. Sharma, Y. Liu, and G. Mademlis, "Balancing peak-torque and drive-cycle efficiency with magnet dimensioning of permanent magnet synchronous machines," in *Proc. IECON 46th Annu. Conf. IEEE Ind. Electron. Soc.*, Oct. 2020, pp. 883–888.
[51] J. Tang, "Synchronous machines with high-frequency brushless excitation for vehicle applications," Ph.D. dissertation, Chalmers Univ. Technol., Sweden, 2019.

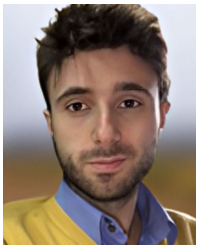

Luca Boscaglia (Member, IEEE) received the B.Sc. degree in electrical engineering from the University of Napoli Federico II, Naples, Italy, in 2015, and the M.Sc. degree in electrical engineering from the Politecnico di Torino, Turin, Italy, in 2019. He is currently pursuing the Ph.D. degree with the Chalmers University of Technology, Göteborg, Sweden, focusing on electromagnetic, mechanical, and thermal design of electrical machines for vehicle applications.

He joined the Research and Development at ABB Low Voltage Motors and Generators, Vittuone, Milan, in 2019, working on thermal design and fluid dynamics computations of electrical machines.

Hari Sankar Natesan Sugumar was born in Dindigul, India, in 1996. He received the bachelor's degree in electrical and electronics engineering from the Thiagarajar College of Engineering, Tamil Nadu, India, in 2017. He is currently pursuing the M.Sc. degree in electric power engineering and electromobility with the Chalmers University of Technology, Gothenburg, Sweden.

From 2017 to 2022, he was at TVS Motor Company Ltd., Hosur, India, as a New Product Development Quality Engineer, handling the development, validation, and approval of key powertrain components (Traction motor, motor controller, vehicle controller, and Charger and 12 V auxiliary electrical parts) of TVS i-Qube electric scooter.

Nimananda Sharma (Member, IEEE) received the B.Tech. degree in electrical engineering from the National Institute of Technology, Silchar, India, in 2011, and the M.Sc. and Ph.D. degrees in electric power engineering from the Chalmers University of Technology, Gothenburg, Sweden, in 2017 and 2022, respectively.

He is currently a Post-Doctoral Researcher with the Electric Machines and Power Electronics Research Group, Chalmers University of Technology. His research interests include design, modeling, and control of electric drives.

Yujing Liu (Senior Member, IEEE) received the B.Sc., M.Sc., and Ph.D. degrees in electrical engineering from the Harbin Institute of Technology, Harbin, China, in 1982, 1985, and 1988, respectively.

From 1996 to 2013, he worked at ABB Corporate Research, Västerås, Sweden. Since 2013, he has been a Professor of electrical power engineering with the Chalmers University of Technology, Gothenburg, Sweden. His research interests include research on motors, converters, wireless charging for electric vehicles, generators, power electronics for tidal power conversion, and high-efficiency machines for energy saving in industrial applications.

Prof. Liu is a member of Swedish Standard Committee on Electrical Machines